Journal of Nuclear Materials 399 (2010) 41–54

Contents lists available at ScienceDirect

Journal of Nuclear Materials

journal homepage: www.elsevier.com/locate/jnucmat

Research on the interfacial behaviors of plate-type dispersion nuclear fuel elements

Qiming Wang, Xiaoqing Yan, Shurong Ding *, Yongzhong Huo

Department of Mechanics and Engineering Science, Fudan University, Shanghai 200433, China

ARTICLE INFO

Article history:
Received 21 July 2009
Accepted 1 January 2010

ABSTRACT

The three-dimensional constitutive relations are constructed, respectively, for the fuel particles, the metal matrix and the cladding of dispersion nuclear fuel elements, allowing for the effects of large deformation and thermal-elastoplasticity. According to the constitutive relations, the method of modeling their irradiation behaviors in ABAQUS is developed and validated. Numerical simulations of the interfacial performances between the fuel meat and the cladding are implemented with the developed finite element models for different micro-structures of the fuel meat. The research results indicate that: (1) the interfacial tensile stresses and shear stresses for some cases will increase with burnup, but the relative stresses will decrease with burnup for some micro-structures; (2) at the lower burnups, the interfacial stresses increase with the particle sizes and the particle volume fractions; however, it is not the case at the higher burnups; (3) the particle distribution characteristics distinctly affect the interfacial stresses, and the face-centered cubic case has the best interfacial performance of the three considered cases.

1. Introduction

Dispersion nuclear fuel elements are widely used in the research and test nuclear reactors because of their high thermal conductivity and high burnup, and they consist of fuel meat and cladding [1]. The fuel meats are similar to particle-reinforced composites in the configurations, distinguished by having a fissile material (such as compounds of uranium or plutonium) dispersed as small particles through a non-fissile matrix of metal, ceramic or graphite. The cladding is made of metal alloy [2,3], such as the aluminum alloy, the zircaloy or the stainless steel.

In the nuclear reactors, the dispersion nuclear fuel elements are subjected to complex loadings: (1) nuclear fissions in the fuel particles lead to heat generation within them, the generated heat is taken away by the flowing coolant water through heat exchanges mainly at the two plate surfaces and the steady-state temperature of the coolant water keeps about 573 K in pressurized-water reactors; (2) solid and gaseous fission products will induce fuel particle swelling; (3) the fission gases would migrate to the free volumes with rise of burnup, and they would form the bubble nucleus if caught by flaws, dislocation, and cavity on the grain boundary, then the bubbles would grow with absorption of the liberated fission gas [4]. The nuclear experiment [5] showed that the miniflaws which were formed at the interface between the fuel meat and the cladding in the production of the nuclear fuel element would develop with the fuel swelling and fission gas release. Consequently, the interfacial facture or delamination between the fuel meat and the cladding is a typical damage form of the dispersion fuel element, in which the irradiation swelling and the fission gas release are the important factors. Furthermore, it was obtained by the nuclear experiment [6] that the interfacial mechanical performance of dispersion nuclear elements were intensely affected by the sizes, the volume fractions and the distribution forms of the fuel particles. Adding to the complexities mentioned above, the fuel particles might not be evenly distributed, which makes the structures of dispersion fuels very complicated and further increases the research difficulty.

Besides the experimental research, numerical simulation is becoming an important tool to explain the experimental results and carry out optimal design. Recently, the relative researches on the dispersion fuel plate with the finite element method (FEM) came forth and some specific codes for the thermal and thermal–mechanical analysis were developed and were being upgraded, including FASTDART [7,8], PLATE [9,10], MAIA [11,12] and DART-TM [13] and so on. In these studies, the dispersion fuel meat was generally treated as homogeneous and the modeling was two-dimensional, that is, the mutual actions between the fuel particles and the matrix, and the mutual actions among fuel particles were not taken into account. Van Duyn [14] studied the PuO_2–Zr dispersion rod-like fuel element with FEM, taking account of the distribution of the fuel particles more actually, while the simulation was relatively simple. Shurong Ding [15,16] studied the thermal and mechanical behaviors of the plate-type dispersion nuclear fuel element, but did not draw the actual cladding structure into consideration. And the study of the effects of the micro-structures on the thermal–mechanical behaviors and the interfacial behaviors is limited.

* Corresponding author.
E-mail address: dsr1971@163.com (S. Ding).

0022-3115/$ - see front matter © 2010 Elsevier B.V. All rights reserved.
doi:10.1016/j.jnucmat.2010.01.001

For the dispersion nuclear fuel plates, the thermal–mechanical behaviors of the fuel elements are induced by the high temperature differences between the steady-state temperature and the room temperature at the initial stage of burnup; and with increasing burnup, the irradiation swelling of the fuel particles will result in intense mechanical interaction between the fuel particles and the matrix. Thus, in numerical simulation of the in-pile mechanical behaviors of dispersion nuclear fuel elements, the effects of large deformation and thermal-elastoplasticity should be introduced in the used three-dimensional constitutive relations.

In this study, the three-dimensional constitutive relations are constructed, respectively, for the fuel particles, the metal matrix and the cladding, allowing for the effects of large deformation and thermal-elastoplasticity. According to the constitutive relations, the method of modeling the irradiation behaviors of dispersion nuclear fuel elements in ABAQUS is developed and it is validated through comparison of the obtained numerical results with the theoretical ones. Besides, considering the micro-structures of plate-type dispersion nuclear fuel elements, the three-dimensional Representative Volume Element is chosen to act as the research object, which might simulate not only the micro stress and strain fields but also the macro deformation along the thickness and the interfacial stresses between the fuel meat and the cladding. In order to clarify the cracking mechanism of the interface and carry out optimal design, numerical simulations of the interfacial mechanical behaviors induced by the irradiation swelling together with the thermal effects are performed with the developed finite element models for different micro-structures of the fuel meat (such as the particle size, the particle volume fraction and the particle distribution forms). And the effects of the micro-structures of the fuel meat on the interfacial stresses are investigated.

2. Development of the three-dimensional constitutive relations

At the initial stage of burnup, the thermal–mechanical behaviors are mainly induced by the high temperature differences. This will result in existence of plastic deformations at the metal matrix and cladding, however, the total deformations remain small. So, at this stage the thermal-elastoplastic constitutive behaviors for small deformation can be adopted for the metal matrix and the cladding, while the thermal-elastic constitutive relation is suitable for the fuel particles.

With increasing burnup, at higher burnups the relative volumetric variations of the particles due to the fission products can reach 20%. Then the mechanical interactions between the fuel particles and the matrix will be enhanced and large deformation can appear. In the three-dimensional constitutive relations for the fuel particles, the matrix and the cladding, finite strain forms should be considered. Besides, when the volumes of the fuel particles enlarge, the configuration of the fuel element will also change accordingly, for example, the plate thickness will increase. This will lead to variations of the heat transfer coefficient between the plate surface and the coolant water and variations of the temperatures within the fuel element. Based on the above reasons, the thermal strain component should be involved in the large-deformation constitutive relations.

For the fuel particles, the internal large strain is mainly induced by the swelling strain and the thermal strain; for the metal matrix or the cladding, their internal large strains mainly result from the plastic component and the thermal component. Therefore, the Prantle–Reuss theory [17] can still be used here. The total deformation rate within the fuel particle is assumed to be the sum of the elastic one, the swelling one and the thermal one; and the deformation rate within the metal matrix or the cladding is supposed to consist of the elastic one, the plastic one and the thermal one. The three-dimensional constitutive relations at higher burnups are deduced in this section; besides, the material parameters needed in the thermal–mechanical analysis are also given. Firstly, the empirical formulas for the particle swellings are given as follows.

2.1. The empirical formula for irradiation swelling of the fuel particles

The fuel particle swelling is usually characterized by the relative volume variations. A kind of swelling coefficient β_V can be introduced as the volumetric swelling rate by

$$SW(BU) = \frac{\Delta V}{V_0} = \int_0^{BU} \beta_V d(BU) \tag{1}$$

where V_0 is the reference volume, ΔV is the volume variation measured after a period of fission reactions. BU is called burnup with the unit % FIMA which is defined as the ratio of the number of the fissioned U atoms to the original number of U atoms, being widely used to characterize the extent of the fission reactions in the nuclear fuel.

The swelling rate β_V (swelling per % FIMA) has three contributions from the fission gas-bubbles β_V^{gs}, the solid fission products β_V^{ss} and the fission densification β_V^{ds}. Namely,

$$\beta_V = \beta_V^{gs} + \beta_V^{ss} + \beta_V^{ds} \tag{2}$$

All the swelling rates have been studied extensively in the literatures and are generally rather complicated. For our FEM calculations, the following simplified relations [18–20] for UO_2 in PWRs will be used.

$$\beta_V^{gs} = 1.122 \times 10^3 \exp(-1.645 \times 10^4/(T-100)) \tag{3}$$

$$\beta_V^{ss} = 6.4 \times 10^{-3} \tag{4}$$

$$\beta_V^{ds} = -[0.51\exp(-59.9 \times BU) + 4.76 \times 10^{-2}\exp(-10.07 \times BU)] \tag{5}$$

where T is the temperature in Kelvin. Note that β_V^{gs} is temperature-dependent and β_V^{ds} is burnup-dependent.

2.2. The three-dimensional constitutive relation for the fuel particles

Considering the temperature variation, the total deformation rate within the fuel particle is assumed to be the sum of the elastic one, the swelling one and the thermal one as

$$d_{kl} = d_{kl}^e + d_{kl}^{sw} + d_{kl}^{th} \tag{6}$$

where d_{kl}^{sw} is the swelling deformation rate. In fact, it is the instantaneous variation rate of the swelling true strain at the current configuration. Because the irradiation swelling only brings volumetric variation without shape changes, the swelling strain is similar to the thermal expansion strain for the isotropic material. That is, only the normal strain e^{sw} which is the same along all directions exists without the shear strain.

According to the definition of irradiation swelling as Eq. (1), the swelling at time t can be expressed as

$$SW(t) = SW[BU(t)] = \frac{\Delta V_t}{V_0} = \frac{V_t - V_0}{V_0} \tag{7}$$

Then the volume at time t is obtained as

$$V_t = [1 + SW(t)]V_0 \tag{8}$$

The variation rate of the absolute volume is

$$\dot{V}_t = \frac{dV_t}{dt} = \frac{dSW(t)V_0}{dt} = \frac{\partial SW(BU)}{\partial(BU)}\frac{dBU(t)}{dt}V_0 = \beta_V(BU)\cdot B\dot{U}\cdot V_0 \tag{9}$$

where $B\dot{U}$ is the burnup rate, that is the burnup per time, which can be obtained by the fission rate. The relative volume variation rate with respect to the volume at time t becomes

$$\frac{\dot{V}_t}{V_t} = \frac{dV_t}{V_t dt} = \frac{\beta_V(BU)}{1 + SW(BU)} B\dot{U} \tag{10}$$

Under the condition of small deformation, we have

$$\frac{dV_t}{V_t} = 3de^{sw} \tag{11}$$

where de^{SW} is the increment of the swelling true strain from time t to time $t + dt$. Then the swelling deformation rate with respect to the current configuration can be acquired as

$$d_{kl}^{sw} = \delta_{kl} \frac{d\varepsilon^{sw}}{dt} = \delta_{kl} \frac{\beta_V(BU)}{3[1 + SW(BU)]} B\dot{U} \tag{12}$$

In practice, the thermal expansion deformation rate is the instantaneous variation rate of the thermal true strain at time t. And the actual expression of true strain can be gained according to the relation between the true strain and the engineering strain, which is given as

$$e = \ln(1 + \varepsilon) = \ln[1 + \alpha_T(T - T_0)] \tag{13}$$

Then the thermal deformation rate at time t can be obtained as

$$d_{kl}^{th} = \delta_{kl}\dot{e} = \delta_{kl} \frac{\dot{\alpha}_T(T - T_0) + \alpha_T \dot{T}}{1 + \alpha_T(T - T_0)} \tag{14}$$

In Eqs. (13) and (14), α_T is the secant thermal expansion coefficient for time t (with temperature T), which is defined according to the deformation with respect to the original configuration; T_0 is the reference temperature.

The elastic deformation rate satisfies the following relation [17]

$$\sigma_{ij}^{\nabla} = D_{ijkl} d_{kl}^{e} \tag{15}$$

where $\sigma_{ij}^{\nabla J}$ is the Jaumann rate of the Cauchy stress tensor, D_{ijkl} is the tangent stiffness tensor of the Jaumann rate [17].

According to Eqs. (6), (12), (13), and (15), the three-dimensional constitutive relation for the fuel particles can be deduced as

$$\sigma_{ij}^{\nabla} = D_{ijkl}\left(d_{kl} - \delta_{kl} \frac{\beta_V(BU)}{3[1 + SW(BU)]} B\dot{U} - \delta_{kl} \frac{\dot{\alpha}_T(T - T_0) + \alpha_T \dot{T}}{1 + \alpha_T(T - T_0)}\right) \tag{16}$$

2.3. The three-dimensional constitutive relations for the metal matrix or the cladding

At the increasing stage of burnup, allowing for the temperature variation, the deformation rate within the metal matrix or the cladding is supposed to consist of the elastic one, the plastic one and the thermal one, that is

$$d_{kl} = d_{kl}^{e} + d_{kl}^{p} + d_{kl}^{th} \tag{17}$$

where the thermal deformation rate is

$$d_{kl}^{th} = \delta_{kl}\dot{e} = \delta_{kl} \frac{\dot{\alpha}_T(T - T_0) + \alpha_T \dot{T}}{1 + \alpha_T(T - T_0)} \tag{18}$$

The elastic deformation rate and the Jaumann rate of the Cauchy stress obey the hypo-elastic relation [17]:

$$\sigma_{ij}^{\nabla} = D_{ijkl} d_{kl}^{e} \tag{19}$$

The plastic flow rule is as follows

$$d_{kl}^{p} = \dot{\lambda} \frac{\partial \psi}{\partial \sigma_{kl}} \tag{20}$$

where $\dot{\lambda}$ is the scalar plastic flow rate, ψ is the plastic flow potential. If the plastic flow potential is associated, the plastic flow potential ψ is the same to the equation of the yield surface. For the strain-hardening material, Eq. (20) demonstrates that the vector of the plastic deformation rate is along the outer normal direction of the yield surface.

The Mises isotropic yield rule can be expressed as

$$\bar{\sigma} = H(\bar{e}_p, T) \tag{21}$$

The corresponding yield surface equation becomes

$$F = f(\bar{\sigma}, \bar{e}_p, T) = \bar{\sigma} - H(\bar{e}_p, T) \tag{22}$$

where $\bar{\sigma}$ is the Mises equivalent true stress, $\bar{e}_p$ is the equivalent plastic true strain. For the large-deformation analysis, the yield surface equation must be expressed with the true stress and the true strain. $\bar{\sigma} = \sqrt{\frac{3}{2} s_{ij} s_{ij}}$, s_{ij} are the components of the deviatoric tensor of the Cauthy stress.

According to the associated flow rule, the plastic deformation rate is given as

$$d_{ij}^{p} = \dot{\lambda} \frac{\partial F}{\partial \sigma_{ij}} = \dot{\lambda} \frac{\partial \bar{\sigma}}{\partial \sigma_{ij}} \tag{23}$$

According to the plastic work rate as

$$\dot{W}_p = \sigma_{ij} d_{ij}^{p} = \bar{\sigma}\dot{\bar{e}}_p \tag{24}$$

together with $\bar{\sigma} = \sqrt{\frac{3}{2} s_{ij} s_{ij}}$, $s_{ij} = \sigma_{ij} - \delta_{ij}\sigma_m$ and $\sigma_m = \frac{1}{3}\sigma_{ii}$, it can be obtained that $\dot{\lambda} = \dot{\bar{e}}_p$.

Thus, the plastic deformation rate (23) can also be expressed as

$$d_{ij}^{p} = \dot{e}_p \frac{\partial \bar{\sigma}}{\partial \sigma_{ij}} \tag{25}$$

According to the yield surface equation as Eq. (22) and the consistent condition (that is, the point located at the yield surface will remain at the yield surface through the plastic loading.), we have

$$\dot{F} = \frac{\partial \bar{\sigma}}{\partial \sigma_{ij}} \dot{\sigma}_{ij} - \frac{\partial H}{\partial \bar{e}_p} \dot{\bar{e}}_p - \frac{\partial H}{\partial T} \dot{T} = 0 \tag{26}$$

Using Eqs. (17), (18), (23), and (25) yields

$$\sigma_{ij}^{\nabla} = D_{ijkl}\left(d_{kl} - \dot{\bar{e}}_p \frac{\partial \bar{\sigma}}{\partial \sigma_{kl}} - \delta_{kl} \frac{\dot{\alpha}_T(T - T_0) + \alpha_T \dot{T}}{1 + \alpha_T(T - T_0)}\right) \tag{27}$$

The Mises yield function is the isotropic function of the stresses, thereby it is the function of the invariant of the stresses. So, the following relation is obeyed [17]

$$\frac{\partial \bar{\sigma}}{\partial \sigma_{ij}} \dot{\sigma}_{ij} = \frac{\partial \bar{\sigma}}{\partial \sigma_{ij}} \sigma_{ij}^{\nabla} \tag{28}$$

Substituting Eqs. (28) into (26) gets

$$\frac{\partial \bar{\sigma}}{\partial \sigma_{ij}} \sigma_{ij}^{\nabla} - \frac{\partial H}{\partial \bar{e}_p} \dot{\bar{e}}_p - \frac{\partial H}{\partial T} \dot{T} = 0 \tag{29}$$

Substitution of Eqs. (27) into (29) yields

$$\dot{\lambda} = \dot{\bar{e}}_p = \frac{\frac{\partial \bar{\sigma}}{\partial \sigma_{ij}} D_{ijkl} d_{kl} - \frac{\partial \bar{\sigma}}{\partial \sigma_{ij}} D_{ijkk} \frac{\dot{\alpha}_T(T - T_0) + \alpha_T \dot{T}}{1 + \alpha_T(T - T_0)} - \frac{\partial H}{\partial T} \dot{T}}{\frac{\partial \bar{\sigma}}{\partial \sigma_{ij}} D_{ijkl} \frac{\partial \bar{\sigma}}{\partial \sigma_{kl}} + \frac{\partial H}{\partial \bar{e}_p}} \tag{30}$$

The three-dimensional constitutive relation for the metal matrix can be deduced through substituting Eqs. (30) into (27),

$$\sigma_{ij}^{\nabla} = D_{ijkl}^{ep} d_{kl} + \sigma_{ij}^{\nabla 0} \tag{31}$$

where D_{ijkl}^{ep} is the tangent elastoplastic stiffness tensor which can be denoted as

$$D^{ep}_{ijkl} = D_{ijkl} - D^{p}_{ijkl} = D_{ijkl} - \frac{D_{ijmn}\frac{\partial\bar{\sigma}}{\partial\sigma_{mn}}\frac{\partial\bar{\sigma}}{\partial\sigma_{pq}}D_{pqkl}}{\frac{\partial\bar{\sigma}}{\partial\sigma_{pq}}D_{pqmn}\frac{\partial\sigma}{\partial\sigma_{mn}} + \frac{\partial\bar{H}}{\partial\bar{e}_p}} \tag{32}$$

$$\sigma^{\nabla 0}_{ij} = \frac{D_{ijkl}\frac{\partial\bar{\sigma}}{\partial\sigma_{kl}}\frac{\partial\bar{\sigma}}{\partial\sigma_{pq}}D_{pqmm}\frac{\dot{\alpha}_T(T-T_0)+\alpha_T\dot{T}}{1+\alpha_T(T-T_0)} + D_{ijkl}\frac{\partial\bar{\sigma}}{\partial\sigma_{kl}}\frac{\partial H}{\partial T}\dot{T}}{\frac{\partial\bar{\sigma}}{\partial\sigma_{pq}}D_{pqmn}\frac{\partial\sigma}{\partial\sigma_{mn}} + \frac{\partial\bar{H}}{\partial\bar{e}_p}} - D_{ijkk}\frac{\dot{\alpha}_T(T-T_0)+\alpha_T\dot{T}}{1+\alpha_T(T-T_0)} \tag{33}$$

When the elastic loading or the unloading is carried out, $D^{ep}_{ijkl} = D_{ijkl}$.

Based on the three-dimensional constitutive relations developed in this section, the finite element procedure can be developed to simulate the irradiation behaviors of the dispersion nuclear fuel element.

2.4. The material models

In this section, the material parameters needed in the thermal analysis and structural analysis are given.

2.4.1. Heat conduction analysis parameters

As for the steady-state thermal analysis problems, the thermal conductivities of the fuel particles, matrix and cladding, the fission rates of the fuel particles, the temperature of the periphery fluid, the heat transfer coefficient between the matrix and the periphery fluid will all affect the temperature distributions of the fuel elements.

2.4.1.1. The heat generation rates of fuel particles. The heat generation rate of the fuel particles corresponds to their fission rate. For a certain fission rate, considering that one-time nuclear fission emits 200 MeV of thermal energy and 1 eV = 1.602×10^{-19} J, the corresponding heat generation rate can be calculated. The computation equation is obtained as Eq. (34)

$$\dot{q} = c \cdot \dot{f} \tag{34}$$

where $c = 3.204 \times 10^{-11}$ J/fission is the generated heat energy every fissionning event and $\dot{f}$ is the fission rate of the fuel particles, which depicts the number of fissions per time per volume of the fuel particles.

2.4.1.2. Thermal conductivities of fuel particles. The model of thermal conductivities of fuel particles improved by Lucuta et al. [21] consists of five contributions and can be expressed as

$$K_{UO_2} = K_0 \cdot FD \cdot FP \cdot FM \cdot FR \tag{35}$$

where K_0 is Harding's expression for the thermal conductivity of unirradiated UO_2; *FD* quantifies the effect of dissolved fission products; *FP* describes the effect of precipitated solid fission products; *FM* is the modified Maxwell factor for the effect of the pore and fission-gas bubbles; *FR* characterizes the effect of radiation damage.

2.4.1.3. Thermal conductivities of matrix and cladding. For the Zircaloy matrix and cladding, its thermal conductivity from the room temperature to the melting point can be expressed by [22]:

$$k = 7.51 + 2.09 \times 10^{-2}T - 1.45 \times 10^{-5}T^2 + 7.67 \times 10^{-9}T^3 \tag{36}$$

where T denotes the temperature in Kelvin.

2.4.2. The mechanical parameters of fuel particles

The thermal expansion of UO_2 fuel particles relative to 300 K can be expressed as [18]

$$\Delta l/l_0 = -3.0289 \times 10^{-4} + 8.4217 \times 10^{-6}(T-273) + 2.1481 \times 10^{-9}(T-273)^2 \tag{37}$$

where T denotes the temperature in Kelvin with the application range from 300 K to 1530 K.

The elastic modulus of UO_2 fuel particles can be described as [19]

$$E = 2.26 \times 10^{11}[1 - 1.131 \times 10^{-4}(T-273.15)][1 - 2.62(1-D)] \tag{38}$$

where E is the elastic modulus, whose unit is Pa. T is the temperature in Kelvin and D is the theoretical density (92–98%). In addition, Poisson ratio v is set to be 0.316.

The Misses hardening rule of UO_2 fuel particles is as the following [22]

$$\bar{\sigma} = \begin{cases} 66.9 - 0.0397T + (520.0 - 0.0386T)\bar{\varepsilon}_p & T \leqslant 1200\,^{\circ}\mathrm{C} \\ 36.6 - 0.0144T + (139.5 - 0.0688T)\bar{\varepsilon}_p & T > 1200\,^{\circ}\mathrm{C} \end{cases} \tag{39}$$

where $\bar{\sigma}$ is the Misses equivalent stress, whose unit is kg/mm^2; $\bar{\varepsilon}_p$ is the equivalent plastic strain.

2.4.3. The mechanical parameters of the matrix and cladding

The matrix and cladding adopt the same material Zircaloy. The thermal expansion coefficient [22] is 5.58×10^{-6}/K. The Young's modulus and Poisson's ratio adopt Fisher Model [23]:

$$E = 9.9 \times 10^5 - 566.9 \times (T - 273.15) \times 9.8067 \times 10^4 \tag{40}$$

$$v = 0.3303 + 8.376 \times 10^{-5}(T - 273.15) \tag{41}$$

where E is Young's modulus (Pa), T is temperature in Kelvin and v is Poisson's ratio.

The strain-hardening curve is described as [24]:

$$\sigma = K\varepsilon^n \cdot \left(\frac{\dot{\varepsilon}}{10^{-3}}\right)^m \tag{42}$$

where σ is the true stress, ε is the true strain, n is the strain-hardening exponent, K is strength coefficient and m is strain rate sensitivity exponent. $\dot{\varepsilon}$ is true strain rate. If $\dot{\varepsilon} < 10^{-5}$/s, set $\dot{\varepsilon} = 10^{-5}$/s.

$$K = 1.0884 \times 10^9 - 1.0571 \times 10^6 T \tag{43}$$

$$n = -1.86 \times 10^{-2} + T(7.11 \times 10^{-4} - 7.721 \times 10^{-7}T) \tag{44}$$

$$m = 0.02 \tag{45}$$

where T is temperature in Kelvin with the application range from 300 K to 730 K.

3. Finite element model

3.1. Selection of the Representative Volume Element and the finite element model

Since dispersion nuclear fuels are similar to particle composites in the configuration, the meso-mechanics research thought [25] of particle-reinforced composites can be used for reference. In the particle composite, the method of Representative Volume Element (RVE) [25] is usually adopted. Assuming that the fuel particles are periodically distributed along the length and width directions, a specific RVE is proposed, as illustrated in Fig. 1, where the selected RVE adopts periodical sizes (meso-scale) at the length and width direction and makes use of the actual size (macro-scale) along the thickness direction. Thus, this kind of RVE model might be called a two-scale model.

In the actual modeling, the corresponding RVE should be developed according to the volume fraction, the particle diameter and the distribution patterns of the fuel particles.

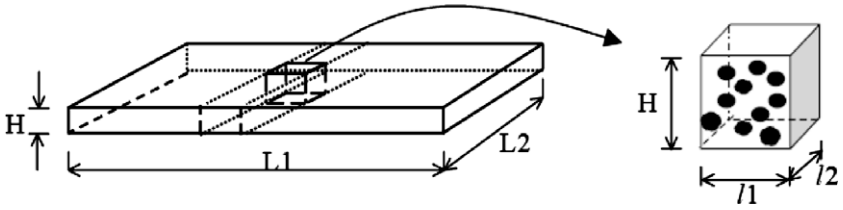

Fig. 1. Dispersion fuel plate and the Representative Volume Element.

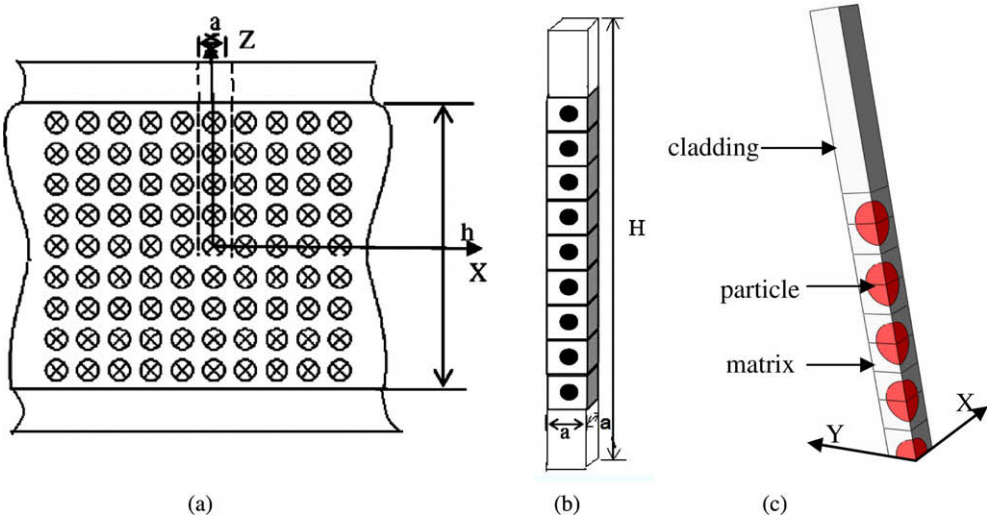

Fig. 2. (a) The sketch map, (b) RVE, (c) finite element model of the dispersion fuel plate.

According to the research thought presented above, the relative simple case is first considered. Assuming that the spherical particles are cubically arranged in the matrix illustrated as Fig. 2a, based on the periodicity and the actual geometry shape that the sizes along the length direction and the width direction are much larger than the one along the thickness, the Representative Volume Element (RVE) is selected as Fig. 2b. For the sake of calculation efficiency, the finite element model is selected according to the symmetry of the RVE to be 1/8 fraction of the RVE, shown as Fig. 2c. The plane $Z = 0$ expresses the midplane of the fuel plate and the plane with $Z = H/2$ denotes the upside surface which is the contact surface with the coolant water. The developed finite element models vary with the micro-structures such as the particle volume fractions, the particle diameters and the particle distribution forms of the fuel meat.

3.2. Mesh grid for the finite element models developed

The meat thickness is set as 1.27 mm and the cladding thickness maintains 0.4 mm. The finite element models for different volume fractions, particle diameters and particle distribution patterns are developed according to the method proposed in the above Section 3.1, supposing that the bonding between the fuel particles and the metal matrix, and the one between the cladding and the fuel meat are perfect. The thermal–mechanical coupling element C3D8RT in the commercial software ABAQUS is used to discretize the finite element models, and the meshes are determined to satisfy the demand of precision.

3.2.1. Finite element models for different volume fractions

The respective finite element models are developed for different particle volume fractions (10%, 20% and 30%) of the fuel meat, with the particle diameter $d = 100$ μm and with the same simple cubic distribution form. The mesh grids, element patterns and the numbers of the nodes and elements are depicted in Fig. 3 and Table 1.

3.2.2. Finite element models for different particle diameters

To evaluate the effect of the particle sizes on the interfacial mechanical behaviors of the dispersion nuclear fuel plate, the finite element models for different particle diameters (50 μm, 100 μm and 200 μm) are developed, with the particle volume fraction being 20% and the particle distribution form being simple cubic. And their mesh information is presented in Fig. 4 and Table 2.

Fig. 3. Finite element models for different volume fractions: (a) 10%, (b) 20% and (c) 30%.

Table 1
Element information for finite element models with different volume fractions.

Volume fraction (%)	Element pattern	Number of elements	Number of nodes
10	C3D8RT	18155	21334
20	C3D8RT	23448	27727
30	C3D8RT	28515	32847

Fig. 4. Finite element models for different particle diameters: (a) 50 μm, (b) 100 μm and (c) 200 μm.

Table 2
Element information for finite element models with different particle diameters.

Particle diameter (um)	Element pattern	Number of elements	Number of nodes
50	C3D8RT	27007	31752
100	C3D8RT	23448	27727
200	C3D8RT	18408	21592

3.2.3. Finite element models for different particle distribution patterns

In order to examine the effect of the particle distribution forms, three distribution patterns (simple cubic (SC), body-centered cubic (BCC) and face-centered cubic (FCC)) are considered, whose distribution patterns are similar to the characteristic crystal cell structures. The finite element models are displayed in Figs. 5 and 6, respectively, with the particle volume fraction being 30% and the particle diameter being 100 μm, and the element information is shown in Table 3.

3.3. Boundary conditions

Since the mechanical analysis in this work is coupled with the thermal analysis, two sets of boundary conditions should be taken into account at the same time. The boundary conditions to determine the temperature field are given as

(1) Except the upside surface $Z = H/2$, the other surfaces of the finite element models all satisfy: $-k\frac{\partial T}{\partial n} = 0$.
(2) The upside surface $Z = H/2$ satisfy the convection boundary condition: $-k\frac{\partial T}{\partial n} = h(T - T_f)$, where the temperature of the periphery fluid T_f is 573 K and the heat transfer coefficient used is 2×10^{-2} W/mm^2 K.

The used boundary condition to determine the stress field is as follows:

(1) The symmetric boundary condition is applied at all the surfaces of the finite element models, except the upside surface $Z = H/2$.
(2) The continuous displacement conditions are met at the interfaces between the fuel particles and the matrix and the one between the meat and the cladding.

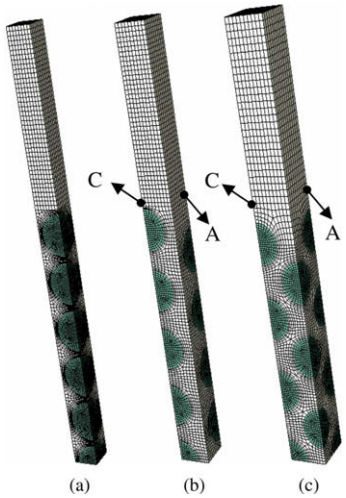

Fig. 6. Finite element models for different particle distributions: (a) SC, (b) BCC and (c) FCC.

Table 3
Element information for finite element models with different particle distribution.

Particle distribution pattern	Element pattern	Number of elements	Number of nodes
SC	C3D8RT	28515	32847
BCC	C3D8RT	26971	30489
FCC	C3D8RT	24400	28683

4. A Simulation method of the in-pile behaviors

4.1. Development of the simulation method in ABAQUS

As mentioned above in Section 2, the total burnup can be divided into two stages: the initial stage of burnup and the

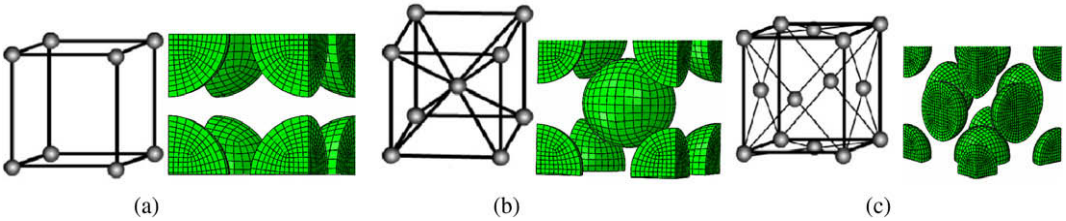

Fig. 5. Several typical crystal cell structures: (a) SC, (b) BCC and (c) FCC.

increasing stage of burnup. At the initial stage of burnup, the mechanical behavior is mainly induced by the temperature difference between the steady-state one and the room one. And with increasing burnup, the irradiation swelling is the main factor to result in variation of the mechanical behaviors. Thus, the loadings should be separated into two steps. It is easy to model the mechanical behaviors at the initial stage of burnup. Firstly, the steady-state temperature field is solved, and then the displacement field, the strain field and the thermal stress field resulting from the temperature differences can be calculated. In ABAQUS, the thermal–mechanical element **C3D8RT** can be chosen, the thermal and thermal–mechanical behaviors can be solved directly. However, the irradiation-swelling simulation with increasing burnup becomes a key problem at the second stage. As is mentioned in the above section, the complexity consists in that: (1) the particle swelling will lead to appearance of large strains in the metal matrix and variation of the configuration of the fuel plate; (2) the changed configuration will bring the temperature variations within the fuel plate.

The emphasis and difficulty were transferred to the introduction of the irradiation swelling of the fuel particles. According to Eqs. (1)–(5) and Eq. (12), the irradiation swellings and the corresponding swelling deformation rates are theoretically worked out as Fig. 7 under the temperature around 600 K. Through computation, it can be found that: (1) when the burnup is less than 2% FIMA, the swelling is less than zero; this is for the reason that the fission densification plays the main role; (2) with increasing burnup to 30% FIMA, the irradiation swelling will reach 17.2%. It can be obtained from the swelling model expressed as Eqs. (1)–(5) that the fission densification has an exponent attenuation with burnup; besides, the gaseous swelling under lower temperatures is a small contribution and the dominant swelling from the solid fission products is a constant. Thus the irradiation swelling depicted in Fig. 5a takes on a nearly linear relation with the burnup. And it can be observed that the swelling deformation rate calculated through Eq. (12) decrease with burnup and it is burnup-dependent or time-dependent.

In ABAQUS, introduction of the irradiation swelling can be implemented by inputting a constant volumetric swelling strain rate of the fuel particle. It is difficult to simulate the real-time swelling strain rate. Since the strength and stiffness issues are mostly concerned at the higher burnups and the other effects are needed to be known about, this problem is simplified through the method of introducing the virtual volumetric swelling strain rate.

Firstly, the irradiation swelling at a certain burnup $SW(BU)$ is calculated out, then the relation between the irradiation swelling and the virtual volumetric swelling strain rate is developed as the following.

The irradiation swelling of the fuel particles at a certain burnup is defined as the relative volumetric change:

$$SW(BU) = \frac{\Delta V}{V_0} \tag{46}$$

where BU denotes burnup (% FIMA), which depicts the ratio of the fissioned atoms to the total fissionable atoms, ΔV is the absolute volumetric change, V_0 is the initial volume.

Owing to the intense mechanical interactions between the fuel particles and the metal matrix induced by the irradiation swelling, the large deformation finite element method is adopted and the Updated Lagrange Method is used. The calculation at a certain burnup should be divided into several time steps and the configurations of the finite element models are updated after every time step. Thus, the volumetric swelling strain rate at every time step is corresponding to the updated configuration. As a result, the simulation method is proposed as follows.

The total calculation process is divided into n virtual time steps, ensuring that the strain increment and deformation at every time step are small. At an arbitrary time step from time $t-1$ to time t, the ratio of the volume at time t to the volume at time $t-1$ is set to be constant. That is,

$$\frac{V_t}{V_{t-1}} = \frac{V_{t-1} + \Delta V_t}{V_{t-1}} = 1 + \theta \tag{47}$$

where θ denotes the average volumetric strain induced by the irradiation swelling at every virtual time step. Then

$$\frac{V_n}{V_0} = \frac{V_1}{V_0} \cdot \frac{V_2}{V_1} \cdots \frac{V_n}{V_{n-1}} = (1+\theta)^n \tag{48}$$

$$SW(BU) = \frac{V_n - V_0}{V_0} = (1+\theta)^n - 1 \tag{49}$$

Eq. (49) expresses the relationship between the average volumetric strain of every time step and the irradiation swelling at a certain burnup. In order to keep the small strain increment, the total number of the virtual time steps n should be set large enough. In the practical calculation, n is set to a limit value in order that θ tends to be a stable value. Consequently, the average volumetric swelling rate could be introduced

$$\dot{\theta} = \theta / 1 \tag{50}$$

where 1 denotes a virtual time step size.

In view of usage of the thermal–mechanical coupling element, the updated steady-state temperature fields are calculated under the updated configuration of the fuel plate; and the thermal defor-

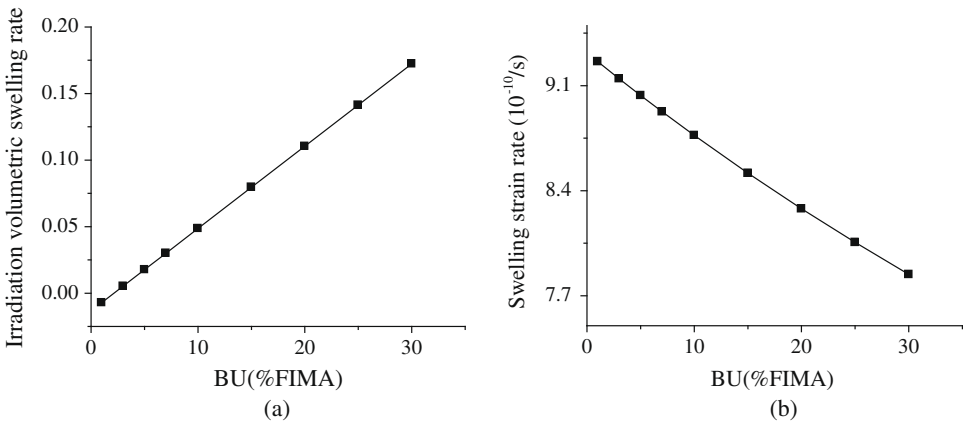

Fig. 7. (a) The irradiation volumetric swelling rate and (b) the swelling deformation rate with increasing the burnup.

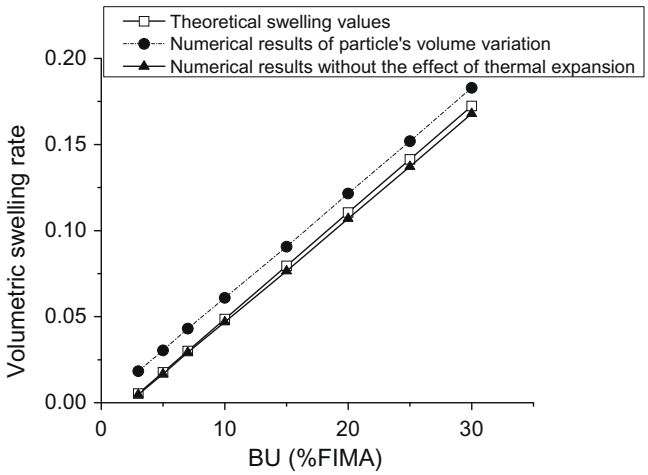

Fig. 8. The comparison of the theoretical results with the numerical simulation ones of the irradiation swelling.

mation rates in Eqs. (14) and (18) can be considered according to the temperature variations.

As a whole, the total computation of the in-pile behaviors is divided into two analysis steps: (1) the first analysis step considered only the thermal effects; this analysis step is further divided into several time steps to calculate the thermal-elastoplastic behavior precisely; (2) the second loading step allows for the contribution of the irradiation swelling. The volumetric swelling strain rate obtained according to Eqs. (47)–(50) is introduced into ABAQUS and enough time steps are divided.

4.2. Validation of the irradiation-swelling simulation

The numerical simulation results of the actual volumetric expansions of the fuel particles (for the case as Fig. 2) at different burnups are compared with the theoretical ones (obtained according to Eqs. (1)–(5)), as denoted in Fig. 8. It can be discovered that the actual volumetric expansion values are slightly higher than the theoretical computation ones; and after eliminating the thermal expansion effect, the obtained volumetric expansion values are very close to and briefly lower than the theoretical ones. This simulation result is reasonable in respect that: (1) the total deformation consists of four parts: the elastic one, the plastic one, the thermal expansion and the irradiation swelling, in which only the elastic deformation, the thermal expansion and the irradiation swelling contribute to the volumetric variation of the fuel particle; (2) the elastic compressive deformation is very small, thus the main contributors of the volumetric variation are the thermal expansion and the irradiation swelling; (3) the volumetric expansion results without the effect of the thermal expansion are lower than the theoretical ones of the irradiation swelling and the differences seem to increase with the burnup, this is for the reason that: (1) the fuel particles are restrained by the metal matrix around to result in the elastic compressive strains within the fuel particles; (2) and the compressive strains increase with burnup.

Based on the above analysis, it can be obtained that the irradiation-swelling simulation with ABAQUS is validated.

5. Results and discussions on the interfacial behaviors

The thermal–mechanical calculations within the burnups ranged from 3% FIMA to 30% FIMA were carried out for the finite element models as displayed in Section 3. The method given in Section 4 is adopted.

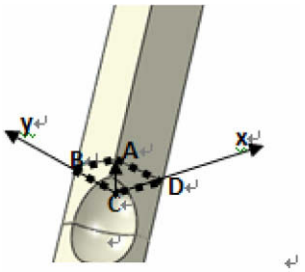

Fig. 9. The interfacial coordinate and the export path CA of the finite element model.

In order to investigate the interfacial mechanical behaviors, the interfacial stresses between the fuel meat and the cladding are focused on, which consist of the interfacial normal stress σ_{zz} and interfacial shear stress $\tau = \sqrt{\tau_{xz}^2 + \tau_{yz}^2}$. The interfacial coordinate and the export path are shown in Fig. 9.

First of all, a simple case is considered (20% volume fraction, fuel particle diameter d = 100 μm, and particle distribution pattern is simple cubic), of which the interfacial stresses at different burnups are shown in Figs. 10 and 11. As depicted in Figs. 10 and 11, the maximum interfacial stresses and its locations all vary with burnup. It can be found that the maximum interfacial normal stresses locate at the two corner points C or A, while the maximum interfacial shear stresses exist between the above two corner points and at high burnups they occur at the middle point between C and A. As a result, the export path from point C to point A is chosen, as shown in Fig. 9.

5.1. Effect of the particle volume fractions

The respective finite element models for different particle volume fractions are developed in Section 3.2.1. The stress fields due to both the thermal effect and the irradiation swelling effect at different burnups are calculated and obtained. The interfacial normal stresses and shear stresses along Export Path CA are shown as Figs. 12 and 13, in which the results corresponding to the thermal effect could be viewed as the ones in the beginning of burnup without considering the irradiation swelling and the relative stresses are only induced by the temperature variations.

Fig. 12 denotes variation of the interfacial normal stress distributions along Path CA for different volume fractions with increasing burnup. It can be found from Fig. 12a that for the 10% volume fraction case the interfacial normal stresses at the location near the point C increase with burnup, while the ones at the location near the point A decrease with burnup. The interfacial normal stresses at point C increase with burnup, while the ones at point A decrease with burnup; and the location of the maximum interfacial normal stresses shift from point A to point C with increasing burnup. Especially, the maximum interfacial normal stress at 30% FIMA increases 50 MPa more than that induced by the thermal effect, and the value is about 3.7 times of the latter.

From Fig. 12b, it can be observed that for the 20% volume fraction case the interfacial normal stresses near Point A increase slightly in the beginning of burnup and then decrease with burnup, and the tensile stresses at the lower burnups become the compressive ones at the higher burnups; however, the interlaminar normal stresses near point C decrease firstly and then increase with burnup, the original compressive stresses change to the tensile ones. At lower burnups, the maximum interfacial normal stresses locate at point A, but when the burnup is higher than 10% FIMA, the maximum points migrate to point C.

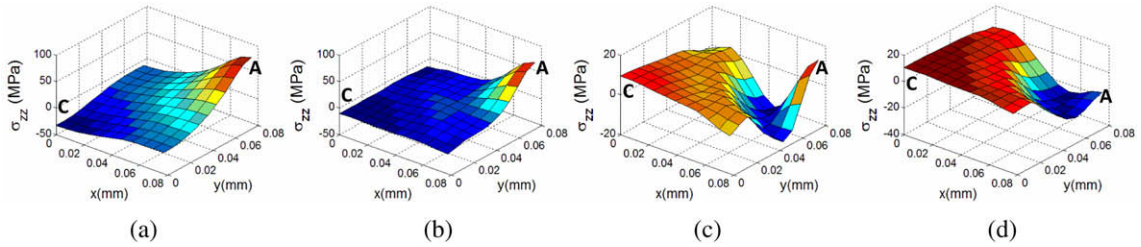

Fig. 10. The interfacial normal stress distributions for the Simple Cubic case at: (a) 3% FIMA, (b) 10% FIMA, (c) 20% FIMA and (d) 30% FIMA.

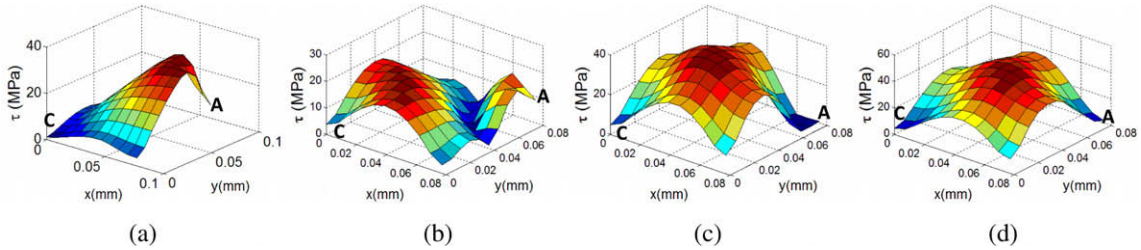

Fig. 11. The interfacial shear stress distributions for the simple cubic case at: (a) 3% FIMA, (b) 10% FIMA, (c) 20% FIMA and (d) 30% FIMA.

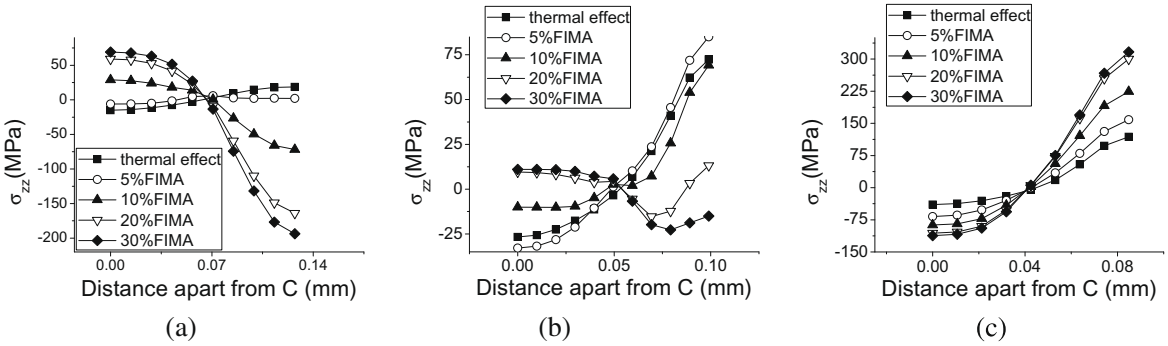

Fig. 12. The interfacial normal stress distributions along Path CA for different volume fractions: (a) 10%, (b) 20% and (c) 30%.

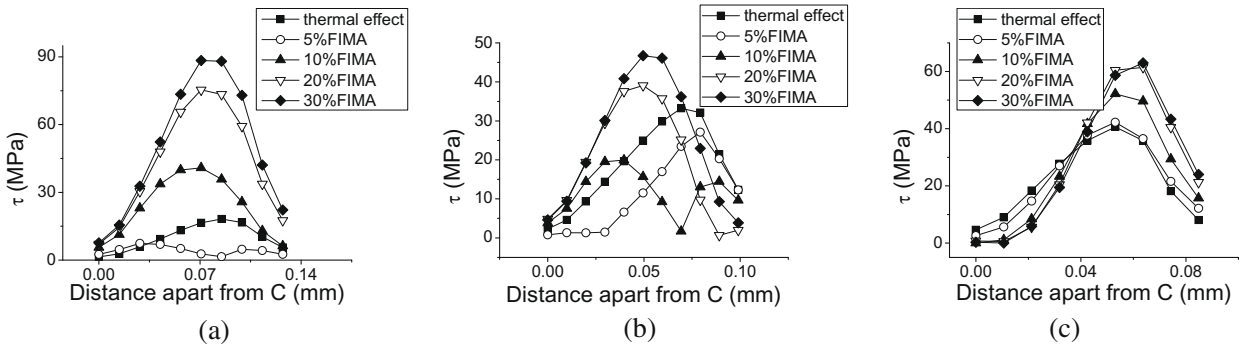

Fig. 13. The interfacial shear stress distributions along Path CA for different volume fractions: (a) 10%, (b) 20% and (c) 30%.

If the particle volume fraction reaches 30% as depicted in Fig. 12c, the interfacial normal stresses near point A increase monotonously with burnup, and the interlaminar normal stresses near point C decrease with burnup; the maximum points always locate at point A. Comparing the maximum interlaminar tensile stress with the result induced by the thermal effect, the maximum interfacial normal stress at 30% FIMA increases by 198 MPa, it is about 1.67 times more than the maximum value due to the thermal effects. As for the three cases in Fig. 12a–c, the intersection points of the curves always locate at the midpoint of Path CA and denote the zero normal stress.

Fig. 13 reveals variation of the interfacial shear stress distributions along Path CA for different volume fractions. As shown in Fig. 13a, it can be found that for the 10% volume fraction case

the interfacial shear stresses first increase and then decrease along Path CA, in which the maximum stress value locates nearby the midpoint. With rise of burnup, the maximum shear stresses along the path decrease first then increase with burnup and approach to the midpoint at higher burnups. Especially, the maximum interfacial shear stress at 30% FIMA increase by 81 MPa more than that at 5% FIMA. From Fig. 13b, it can be observed fundamentally that the similar phenomenon as that of the 10% volume fraction case exists for the 20% volume fraction case. However, if the volume fraction reaches 30% as depicted in Fig. 13c, the maximum interfacial shear stresses increase with burnup, and the maximum points shift slightly toward point A.

As discussed above, the values and locations of the interfacial normal stresses and shear stresses along path CA are presented. In order to evaluate the influence of the fuel volume fraction and burnup on the interfacial stresses clearly, the variation trends of the maximum interfacial normal stresses and shear stresses for different particle volume fractions with rise of burnup are shown in Fig. 14. Since the interfacial tensile strength is generally weaker than the compressive strength for an interface, thus the special concern is drawn to the interfacial tensile stresses between the meat and the cladding, that is, the attention is mainly paid to the maximum interfacial tensile stresses and shear stresses.

Fig. 14a manifests variations of the maximum interfacial normal stresses with the burnup for three volume fraction cases (10%, 20% and 30%). For the 10% volume fraction case, the maximum interfacial normal stresses decrease before 5% FIMA, then increase thereafter despite a smaller increasing rate. Nevertheless, the 20% volume fraction case is different; it is obvious that the maximum interfacial normal stresses increase before 5% FIMA, then decrease with the point of 5% FIMA having the maximum value. At the same time, the 30% volume fraction case presents a monotonously increasing trend although the increasing rate decreases with burnup. Analyzing the effect of the volume fractions, it can be found that before 15% FIMA maximum interfacial normal stresses increase with the volume fractions, whereas after 15% FIMA the maximum interfacial normal stresses follow this ascending order: 20% volume fraction, 10% volume fraction and 30% volume fraction. Particularly, the maximum interfacial normal stress of the 30% volume fraction case is 316.5 MPa, 28.8 times of that of the 20% volume fraction case.

Fig. 14b depicts variation of the maximum interfacial shear stresses with the burnup for three particle volume fraction cases (10%, 20% and 30%). The interfacial shear stresses of the three cases all first decrease then increase with burnup, despite different turning points: the 10% volume fraction case occurs at 5% FIMA, at 10% FIMA for 20% volume fraction and at 3% FIMA for 30% volume fraction. The increasing rates after the turning points of the three cases are also dissimilar: the highest case is the 10% volume fraction one, while the lowest one is the 30% volume fraction case. It can be found from Fig. 14b that: (1) before 7% FIMA, the maximum interfacial shear stresses increase with the particle volume fractions; (2) from 7% FIMA to 17% FIMA, the 30% volume fraction case still has the largest shear stresses, while the second one is the 10% volume fraction case; (3) thereafter, the one of the 10% volume fraction case holds the maximum value which is twice as much as the lowest case the 20% volume fraction case.

5.2. Effect of the particle diameter

The finite element models for the cases with the spherical particle diameters being 50 μm, 100 μm and 200 μm, respectively, are

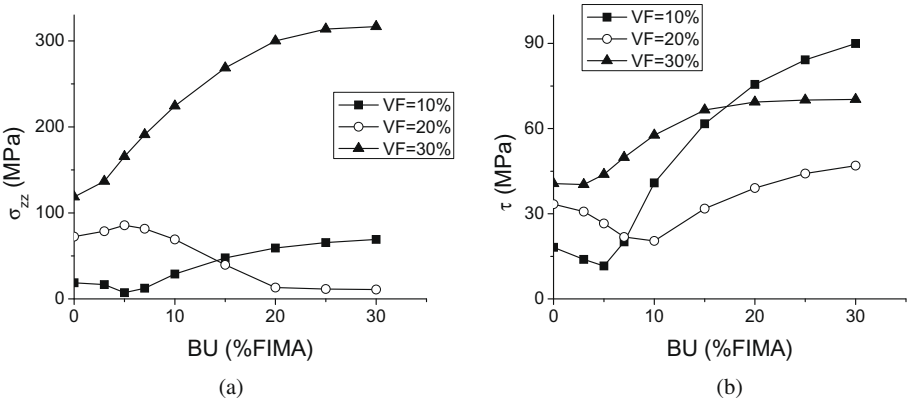

Fig. 14. The maximum interfacial: (a) normal stresses and (b) shear stresses for different volume fractions with rise of the burnup.

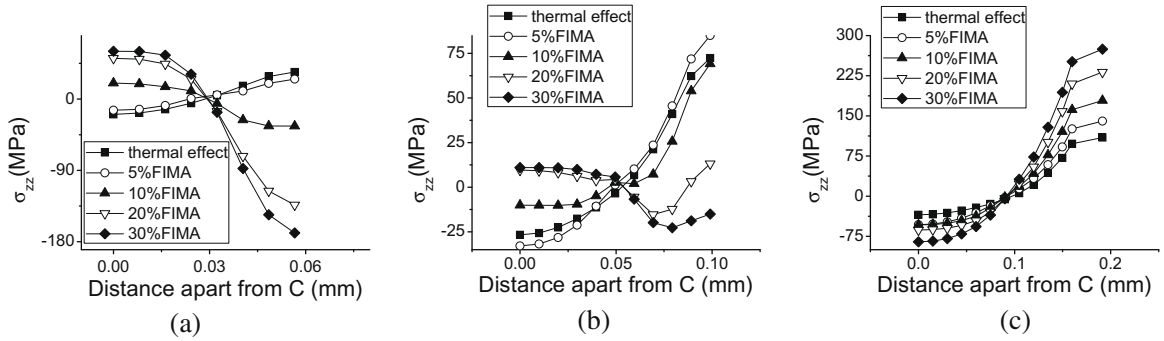

Fig. 15. The interfacial normal stress distributions along path CA for different particle diameters: (a) 50 μm, (b) 100 μm and (c) 200 μm.

developed in Section 3.2.2. The stress fields induced by the thermal effect and the particle swelling at different burnups are worked out. The interfacial normal stresses and shear stresses along Export Path CA are shown in Figs. 15 and 16.

Fig. 15 denotes variations of the interfacial normal stress distributions along Path CA for different particle diameters. For the 50 μm diameter case, the interfacial normal stresses near point C increases with burnup, while those near point A deceases with burnup; the maximum interfacial normal stress locate at point A at lower burnups, whereas the relative maximum values occur at point C at high burnups. The case with the diameter being 100 μm is the same as the 20% volume fraction case discussed in Section 5.1. Fig. 15c displays the 200 μm diameter case, which reveals that the interfacial normal stresses increase monotonously along path CA, and the maximum values at point A increase with burnup. Particularly, the maximum interfacial normal stress at 30% FIMA is 2.5 times of the relative value induced by the thermal effect.

Fig. 16 shows variations of the interfacial shear stress distributions with increasing burnup along Path CA for different particle diameters. It can be found that high interfacial shear stresses locate near the midpoint of the path, and the stress values at the two end points are very low. As for the case shown in Fig. 16a with the particle diameter being 50 μm, the maximum interfacial shear stresses along the path CA increase with burnup, and especially the maximum shear stress at 30% FIMA is about 8 times of the value at 5% FIMA. Similarly, the maximum shear stresses of the 200 μm diameter case increase with burnup, however the region with larger stress values is narrowed and the maximum stress at 30% FIMA is just 1.6 times as large as that under the thermal effect.

Fig. 17 illustrates variations of the maximum interfacial normal stresses and shear stresses with the burnup for different particle diameters. As depicted in Fig. 17a, with increasing burnup, the maximum interfacial normal stresses of the 50 μm diameter case decrease first and then increase smoothly, but for the case with the 100 μm diameter the maximum normal stresses first increase and then decrease. Different from the above cases, the maximum interfacial stresses of the 200 μm diameter case monotonously increase and the maximum stress value at a certain burnup is much larger than the other two cases. Before 15% FIMA, the interfacial normal stresses increase with the fuel particle diameters; while after 15% FIMA the 100 μm diameter case holds a relatively low value.

It can be discovered from Fig. 17b that with increasing burnup the maximum interfacial shear stresses of the three cases all decrease in the beginning and then increase though the variation rates differ. As a result, the effect of the particle diameters on the maximum shear stresses is different at different burnup ranges: before 7% FIMA, the shear stresses increase with the particle diameters; whereas from 7% FIMA to 12% FIMA, the order from having high stress value to holding low value transforms to the 200 μm case, the 50 μm case and the 100 μm case; after 12% FIMA, the 50 μm diameter case transcend the 200 μm diameter case, becoming the case with the maximum interfacial shear stress.

5.3. Effect of the fuel particle distribution

The finite element models for three distribution patterns (simple cubic (SC), body-centered cubic (BCC) and face-centered cubic (FCC)) are considered in Section 3.2.3. The interfacial normal stresses and shear stresses with increasing burnup are presented as

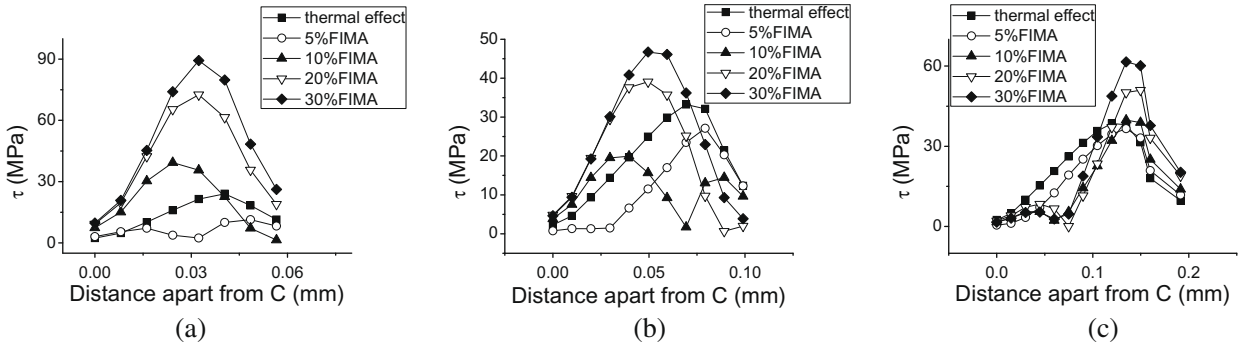

Fig. 16. The interfacial shear stress distributions along path CA for different particle diameters: (a) 50 μm, (b) 100 μm and (c) 200 μm.

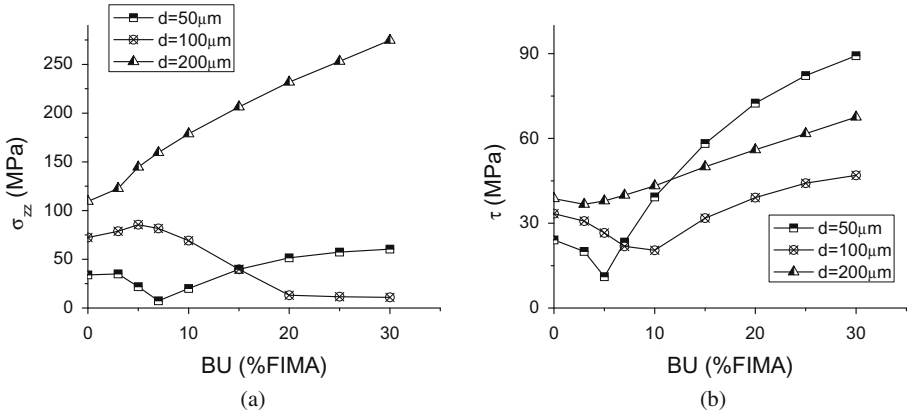

Fig. 17. The maximum interfacial: (a) normal and (b) shear stress with the variation of particle diameter.

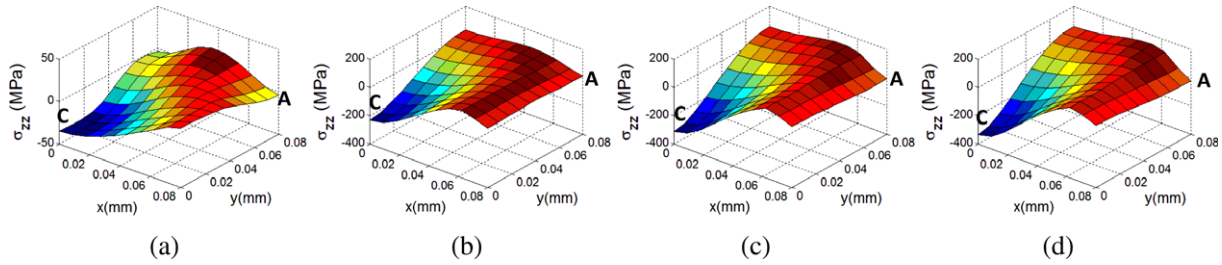

Fig. 18. The interfacial normal stress distributions of the body-centered cubic case at: (a) 3% FIMA, (b) 10% FIMA, (c) 20% FIMA and (d) 30% FIMA.

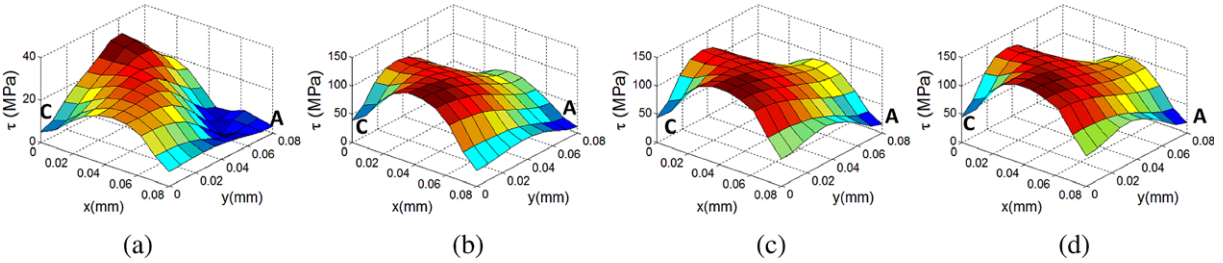

Fig. 19. The interfacial shear stress distributions of the body-centered cubic case at: (a) 3% FIMA, (b) 10% FIMA, (c) 20% FIMA and (d) 30% FIMA.

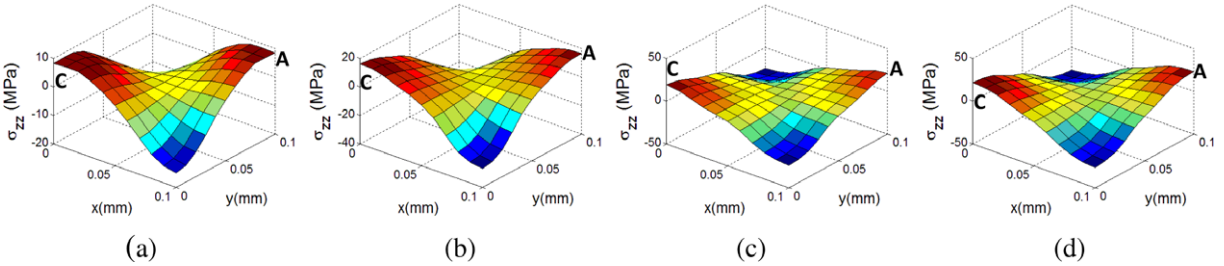

Fig. 20. The interfacial normal stress distributions of the face-centered cubic case at: (a) 3% FIMA, (b) 10% FIMA, (c) 20% FIMA and (d) 30% FIMA.

Figs. 18–21. The effect of the particle distribution forms will be discussed.

It can be found from Figs. 18–21 that the interfacial stress distribution trends of the BCC case and the FCC one all remain fundamentally the same with increasing burnup. As for the BCC case larger interfacial normal stresses are near point A and larger shear stresses are near point C. However, the FCC case takes on a dissimilar distribution: the normal and shear stress distributions are symmetrical against line BD (referred to Fig. 9); the maximum interfacial normal stresses occur nearby the corner point C and A; the three-dimensional plots of the interfacial shear stresses at the interface display certain shapes like cranes.

Fig. 22 depicts the maximum interfacial normal stresses and shear stresses for different particle distribution patterns with increasing burnup. As shown in Fig. 22a, the interfacial normal stresses fundamentally increase with burnup. After 3% FIMA, the maximum interfacial normal stresses and their increasing rates are in the following descending order: the SC pattern, the BCC pattern and the FCC pattern, and the higher the burnup is, the larger the difference exists; especially, when the burnup reaches 30% FIMA, the maximum normal stress of the SC case is about 2.4 times as large as that of the BCC case and about 14 times as large as that of the FCC case. It can be found from Fig. 22b that with increasing burnup, 1) the maximum interfacial shear stresses of the SC case increase smoothly and reach a stable value about 70 MPa; 2) in the beginning, the BCC case has lower interfacial shear stress, but the stress magnitude even becomes 141 MPa at 10% FIMA after the sharp increase from 3% to 10% FIMA; 3) as far as the

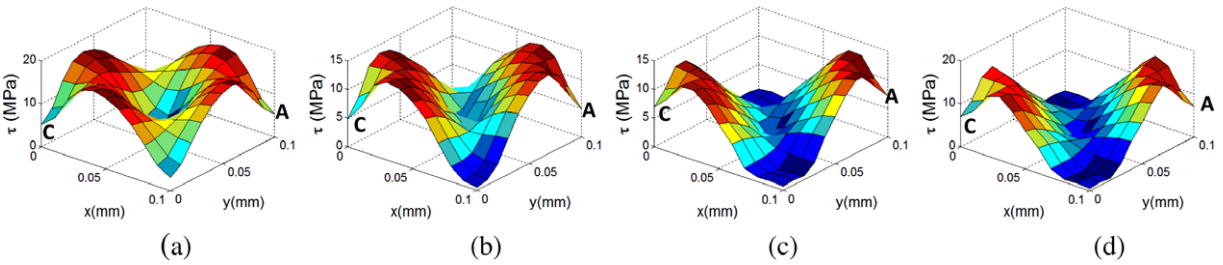

Fig. 21. The interfacial shear stress distributions of the face-centered cubic case at: (a) 3% FIMA, (b) 10% FIMA, (c) 20% FIMA and (d) 30% FIMA.

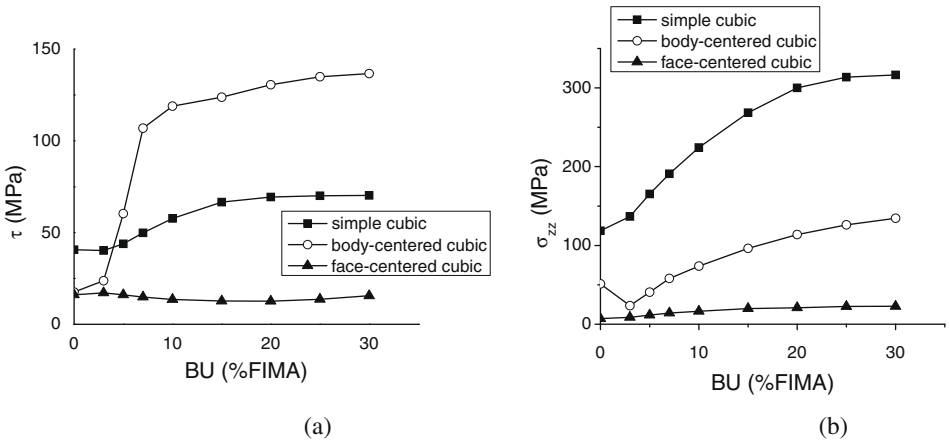

Fig. 22. The maximum interfacial: (a) normal stresses and (b) shear stresses for different fuel particle distribution forms.

FCC case is concerned, it can be observed that the relative stresses remain round 17 MPa till the high burnup. It can also be examined that at the initial stage of burnup the maximum interfacial shear stresses for the considered distribution forms follow the ascending order as: the FCC case, the BCC case and the SC case, while the ascending order is modified to the FCC case, the SC case and the BCC case at higher burnups.

As discussed above, it can be obtained that among the three particle distribution patterns the FCC case has the best interfacial performance.

6. Conclusion

Based on the constructed three-dimensional constitutive relations, a method of modeling the in-pile behaviors of the dispersion fuel element in ABAQUS is developed and validated. Since delamination between the fuel meat and the cladding is a characteristic damage form of the dispersion fuel plates, the interfacial stresses between them are investigated. The effects of the fuel volume fractions, the particle diameters and the particle distributions on the interfacial mechanical performances are evaluated to supply the numerical basis for the fuel element design and operation. The main conclusions can be drawn for the considered parameters:

(1) As for the simple cubic cases with different fuel volume fractions, the regions having the maximum interfacial normal stresses are different from the ones with the maximum interfacial shear stresses. The maximum interfacial normal stresses of the 10% and 30% volume fraction cases increase with burnup, whereas the ones of the 20% volume fraction case decrease with burnup; and the maximum interfacial shear stresses of the three cases all increase with burnup except the ones at the initial stage. Especially, at higher burnups, the maximum normal stresses consist in the case with the highest particle volume fraction; nevertheless the high shear stresses occur in the lowest volume fraction one.

(2) For the simple cubic cases with different particle diameters, the interface locations with the maximum interfacial normal stresses differ from the region with the maximum interfacial shear stresses. The maximum interfacial normal stresses of the 50 μm and 200 μm particle diameter cases increase with burnup, whereas the ones of the 100 μm cases decrease with burnup, and the maximum interfacial shear stresses increase with burnup as a whole. Especially at higher burnups, the highest normal stresses locate in the cases with big particle diameters, while the largest shear stresses exist in the case with the smallest diameter.

(3) Different interfacial stress distributions happen for different particle distribution pattern, and the regions with the maximum interfacial stresses are dissimilar.

(4) For the three considered particle distribution forms, the maximum interfacial normal stresses and shear stresses fundamentally increase with burnup except for the ones at the initial stage. At higher burnups, the maximum interfacial normal stresses are in the ascending order: the simple cubic case, the body-centered cubic case and the face-centered cubic case, whereas the relative order for the shear stresses transfer to: the body-centered cubic case, the simple cubic case and the face-centered case. And according to the results of both the maximum interlaminar normal stresses and the maximum shear stresses, it can be obtained that the face-centered cubic case presents the best interfacial performance.

(5) In order to prevent the interfacial delamination, fracture and the cladding bubbling, the proper parameters such as the fuel volume fractions, the particle diameters and the particle distribution patterns should be chosen to optimize the dispersion fuel element.

Acknowledgements

The authors thank for the supports of the Natural Science Foundation of China (10772049, 10672042), Research and Development Program of China (863 Program, 2009AA04Z408), the Natural Science Foundation of Shanghai (06ZR14009), the Pujiang Scholar Program, and the Wangdao Scholar Program (08076) of Fudan University.

References

[1] A. Leenaers, S. Van Den Berghe, S. Dubois, J. Noirot, M. Ripert, P. Lemoine, Microstructural Analysis of Irradiated Atomized U(MO) Dispersion Fuel in an Al Matrix with Si Addition, RRFM2008 Transactions, Session2: Fuel Development and Fabrication, pp. 106–110.
[2] Enrique. E. Pasqualini, Monolithic UMo Nuclear Fuel Plates with Nonaluminum Cladding, RRFM2008 Transactions, Session2: Fuel Development and Fabrication, pp. 123–127.
[3] J.G. Marques, A.R. Ramos, Core conversion of the Portuguese research reactor to LEU fuel, in: 29th International Meeting on Reduced Enrichment for Research and Test Reactor, Prague, Czech Republic, September 23–27, 2007.
[4] Chan Bock Lee, Yong Sik Yang, Dae Ho Kim, Sun Ki Kim, Je Geun Bang, Journal of Nuclear Science and Technology 45 (1) (2008) 60–71.
[5] M.R. Finlay, Post Irradiation Examination of Monolithic Mini-Fuel Plates from RERTR-6&7, RRFM2007 Transactions, Session III: Fuel Development, pp. 151–156.

[6] S.J. Oh, K.H. Kim, S.J. Jang, D.B. Lee, Y.S. Lee, J.M. Park, H.D. Park, C.K. Kim, The Development of U-7WT.%Mo for Large Particle Powers by Centrifugal Atomization, RRFM2006 Transactions, Session 2: Poster Fuel Development, pp. 136–140.
[7] H. Taboada, J. Rest, M.V. Moscarda, M. Markiewicz, E. Estevez, in: Proceedings of the 24th International Management on Reduced Enrichment for Research and Test Reactors, San Carlos de Bariloche, Argentina, 3–8 November 2002.
[8] J. Rest, The DART Dispersion Analysis Research Tool: A Mechanistic Model for Predicting Fission-Product-Induced Swelling of Aluminum Dispersion Fuels, ANL-95/36, 1995.
[9] S.L. Hayes, M.K. Meyer, G.L. Hofman, J.L. Snelgrove, R.A. Brazener, in: Proceedings of the 2003 International Meeting on Reduced Enrichment for Research and Test Reactors, Chicago, IL, 5–10 October 2003.
[10] S.L. Hayes, G.L. Hofman, M.K. Meyer, J. Rest, J.L. Snelgrove, in: 2002 International Meeting on Reduced Enrichment for Research and Test Reactors, Bariloche, Argentina, 3–8 November 2002.
[11] V. Marelle, S. Dubois, M. Ripert, J. Noirot, P. Lemoine, in: The RERTR-2007 International Meeting on Reduced Enrichment for Research and Test Reactors, Diplomat Hotel – Prague, Prague, Czech Republic, 23–27 September 2007.
[12] V. Marelle, F. Huet, P. Lemoine, in: Proceedings of the Eighth International Topical Meeting on Research Reactor Fuel Management, München, Germany, 21–24 March 2004.
[13] Roberto Saliba, Horacio Taboada, Ma. Virginia Moscarda, in: 2003 International Meeting on Reduced Enrichment for Research and Test Reactors, Chicago, IL, 5–10 October 2003.
[14] Lee Van Duyn, Evaluation of the mechanical behavior of a metal-matrix dispersion fuel for plutonium burning, M.S. Thesis of Georgia Institute of Technology, November 2003.
[15] Shurong Ding, Xin Jiang, Yongzhong Huo, Lin an Li, Journal of Nuclear Materials 374 (2008) 453–460.
[16] Shurong Ding, Yongzhong Huo, XiaoQing Yan, Journal of Nuclear Materials (2009), doi:10.1016/j.jnucmat.2009.04.015.
[17] T. Belytschko, W.K. Liu, B. Moran, Nonlinear Finite Elements for Continua and Structures, John Wiley & Sons Ltd., UK, 2000.
[18] W. Chubb, V.W. Storhok, D.L. Keller, Nuclear Technology 18 (1973) 231–255.
[19] T. Nakajima, M. Ichikawa, et al., FEMAXI-III: A Computer Code for the Analysis of Thermal and Mechanical Behavior of Fuel Rods, AERI-1298, 1985.
[20] W. Wiesenack, M. Vankeerberghen, R. Thankappan, Assessment of UO2 Conductivity Degradation Based on In-pile Temperature Data, HWR-469, 1996.
[21] P.G. Lucuta, H.S. Matzke, I.J. Hastings, Journal of Nuclear Materials 232 (1996) 166–180.
[22] MATPRO-09, A Handbook of Materials Properties for Use in the Analysis of Light Water Reactor Fuel Rod Behavior, USNRC TREE NUREG-1005, 1976.
[23] E.F. Fisher, C.J. Renken, Physical Review 2 (1954) A482–A494.
[24] D.L. Hagrman, G.A. Reyman, MATPRO-Version11, A Handbook of Materials Properties for Use in the Analysis of Light Water Reactor Fuel Rod Behavior, NUREG/CR-0497, TREE-1280, Rev.3, 1979A.
[25] Sreedhar Kari, Harald Berger, Reinaldo Rodriguez-Ramos, Ulrich Gabbert, Composite Structures 77 (2007) 223.